Editors' Suggestion | Featured in Physics

Centrifugal Flows Drive Reverse Rotation of Feynman's Sprinkler

Kaizhe Wang,[1,2] Brennan Sprinkle,[3] Mingxuan Zuo,[1] and Leif Ristroph[1,*]
[1]Applied Math Lab, Courant Institute, New York University, New York, New York 10012, USA
[2]Department of Physics, New York University, New York, New York 10003, USA
[3]Department of Applied Mathematics and Statistics, Colorado School of Mines, Golden, Colorado 80401, USA

(Received 26 December 2022; accepted 6 December 2023; published 26 January 2024)

The issue of reversibility in hydromechanical sprinklers that auto-rotate while ejecting fluid from S-shaped tubes raises fundamental questions that remain unresolved. Here, we report on precision experiments that reveal robust and persistent reverse rotation under suction and a model that accounts for the observed motions. We implement an ultralow friction bearing in an apparatus that allows for free rotation under ejection and suction for a range of flow rates and arbitrarily long times. Flow measurements reveal a rocketlike mechanism shared by the reverse and forward modes that involves angular momentum flux, whose subtle manifestation in the reverse case stems from centrifugal effects for flows in curved conduits. These findings answer Feynman's long-standing question by providing quantitatively accurate explanations of both modes, and they suggest further inquiries into flux-based force generation and the roles of geometry and Reynolds number.

DOI: 10.1103/PhysRevLett.132.044003

Puzzles, paradoxes, and thought experiments in physics play the important role of probing abstract concepts in concrete contexts. An enduring riddle in fluid mechanics popularized by Richard Feynman pertains to a type of auto-rotating lawn sprinkler that spins when fluid is expelled from its S-shaped tubes: Does the sprinkler also rotate if fluid is instead sucked in, and if so, in what direction [1–3]? While flows are certainly irreversible in the inertial regime [4], the consequences for the dynamics of the reverse sprinkler remain unclear. The problem invites reasoning based on fundamental principles while also exposing subtleties, for example, in the application of momentum conservation to systems with sources, sinks, or otherwise open and subject to mass flux and flow throughput [5,6]. The fluid dynamical complexities pertain to flow-structure interactions involving chiral geometries and flows due to suction into orifices [7–10], as jets emitted from moving bodies [11–13], and in curved conduits [14–16], all of which may depend on the strength of driving or Reynolds number.

Conflicting answers to Feynman's question have come from past studies that employ principle-based reasoning and fluid mechanical argumentation. Applications of angular momentum conservation have predicted no rotation [17,18] or reverse rotation opposite to the sense of the forward sprinkler [19,20]. The effects of viscosity and turbulence have been invoked as possible causes of reverse rotation in steady state [20–22]. Other work argues for reverse torques by appealing to the distorted flow and pressure distribution in curved pipes [23]. The challenge of such approaches, and perhaps cause of the disagreements, is they rely on untested assumptions (e.g., state of the flow) and do not furnish testable predictions that would justify the focus on one effect over others.

The thought experiment has been turned into a real one, as done by Feynman and later by others in systems involving S- or L-shaped rigid tubes connected to flexible hosing whose twisting motions are observed [17,24–26]. These studies report a transient effect but no response in steady state. Other experiments employing a central hub mounted on rotary bearings report various outcomes under suction: no steady-state rotation [27,28], steady-state reverse rotation [23,29,30], and unsteady motions including changes in direction [29]. These inconsistencies may be due to bearing friction, which was overcome with a floating sprinkler but whose limited run times did not distinguish transient and steady-state outcomes [31]. Other experiments report rotations of either sense for modified internal geometries [28,30]. Hence, the dynamics may be sensitive to details of the geometry.

Here, we answer Feynman's question through precision experiments on freely-rotating and long-running sprinklers, measurements of their flow fields, and a model whose quantitative predictions are tested and validated. Our approach exploits surface tension effects to both float the sprinkler at the water surface and permit free rotation in response to suction or expulsion. A cut-away view in Fig. 1(a) shows the sprinkler's construction. Arms formed from curved tubes emanate from a cylindrical hub with closed bottom. An external siphon tube is inserted through an opening in the top to withdraw or inject fluid. The annular top breaches the free surface and induces downward-deflected menisci on its inner and outer perimeters. Slight deflections are achieved by adding air to an internal

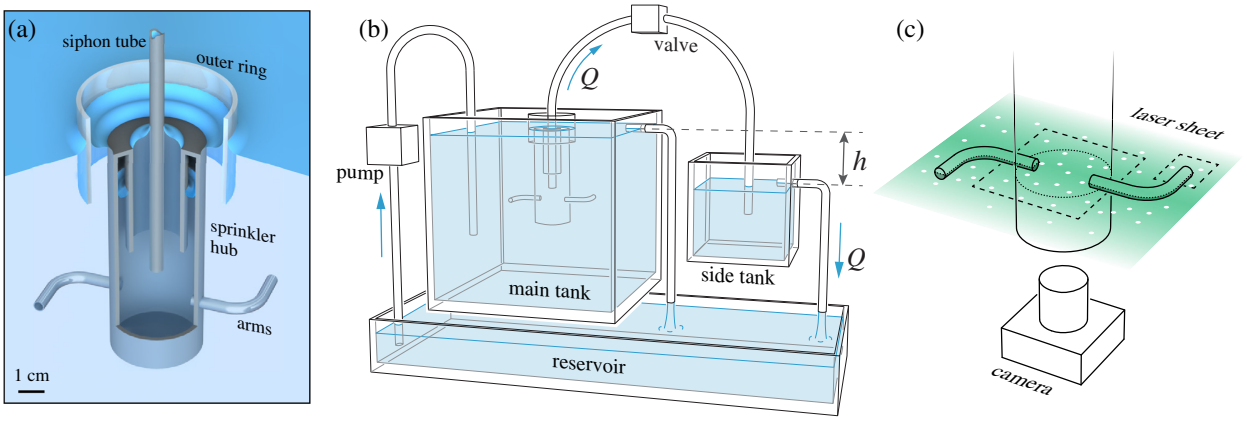

FIG. 1. Experimental setups. (a) Cut-away schematic of the floating sprinkler, which consists of tubular arms connected to a cylindrical hub. Capillary interactions with a siphon tube and outer ring center the sprinkler and allow it to rotate freely. (b) Flow control apparatus (not to scale) operating in suction mode. A siphon draws water through the sprinkler at rate Q, and a valve allows for impulsive start-up. Overflows maintain the levels in the main and side tanks. (c) Flow imaging with a laser sheet illumination of particle-laden water. A camera captures photos and videos in the regions of interest.

cavity of the hub such that the system is slightly negatively buoyant, with surface tension making up the difference to achieve vertical force balance. The downward menisci interact with the upward menisci on the siphon tube and an outer ring, both made of hydrophilic glass. The repulsive interaction between oppositely signed menisci [32–34] ensures that the sprinkler remains stably centered while free to rotate. Thus, the sprinkler is the rotor and the glass surfaces serve as stators in a rotational bearing that, lacking any solid-solid contacts, has extremely low friction. Details of the experimental systems are provided in the Supplemental Material [35].

The surrounding components allow for the control of the flow throughput—both direction (suction or expulsion) and magnitude—as well as time-resolved tracking of the sprinkler's rotation. Figure 1(b) shows the operation under suction. A side tank of lower water level draws fluid through a siphon from the main tank, whose level is maintained by a pump and overspill system. The level in the side tank is also held constant by an overflow that is intercepted for measurement of the volumetric rate Q through the sprinkler. Thus, the system runs indefinitely under constant conditions. The driving pressure is proportional to the difference h in water levels, which is controlled and varied via the height of the side tank. Expulsion is achieved similarly: the siphon flow is reversed by raising the side tank higher than the main tank, with the pump replenishing the former and Q measured from the latter. In both modes, a side-view camera (not shown) images markers on the sprinkler hub to measure the instantaneous rotation rate $\Omega(t)$.

When fluid is expelled from the sprinkler, it rotates in the expected "forward" direction with the orifices of the arms trailing, as shown in Fig. 2(a) and Supplemental Videos 1 and 2 [35]. Displayed as the red curve are representative time series data of the sprinkler's angular velocity for flow that is impulsively started at $t = 0$ and quickly reaches a constant value of $Q = 2.0\ \mathrm{cm}^3/\mathrm{s}$. Steady-state rotation with positive time-averaged angular velocity $\overline{\Omega} > 0$ (red dot) is reached after about a minute, as verified in repeated trials (gray curves). When fluid is instead suctioned in at the same $|Q|$, the sprinkler rotates in "reverse" with $\Omega < 0$ and the orifices leading. The blue curve and associated gray ones show a transient burst followed by a terminal state with significant fluctuations but definitively negative time average $\overline{\Omega} < 0$ (blue dot). The reverse mode is about 40 times slower than the forward, and hence the two cases are displayed with different vertical scales. Videos 3 and 4 show that reverse motion is observed for sprinklers of opposite chirality [35], which indicates that the cause is intrinsic propulsion rather than an external influence (e.g., the Earth's rotation or background flows).

These findings are robust across varying Q or, equivalently, the pipe flow Reynolds number $\mathrm{Re} = 2\rho\overline{V}a/\mu$. Here, ρ and μ are the fluid density and viscosity, respectively, and $\overline{V} = |Q|/2\pi a^2$ is the section-averaged flow speed through each arm of inner radius a. As shown by the plots of the measured $\overline{\Omega}$ in Fig. 2(b), the terminal speed of the forward sprinkler increases quasilinearly with Q or Re. In contrast, the reverse case has opposite sign, uniformly lower magnitudes, stronger relative fluctuations, and a markedly nonlinear trend. For the lowest Re tested, the reverse motion is weak and undirected with $\overline{\Omega} \approx 0$. The potential roles of bearing friction and manufacturing errors are discussed in the Supplemental Material [35].

We propose that both modes of the sprinkler are driven by a common mechanism similar to the classical rocket. This hypothesis is intuitive for the forward case, for which flow visualizations support the view as a rotational analog to the rocket. Video 5 and the photograph of Fig. 3(a) are obtained by adding green dye to the supplied fluid, which

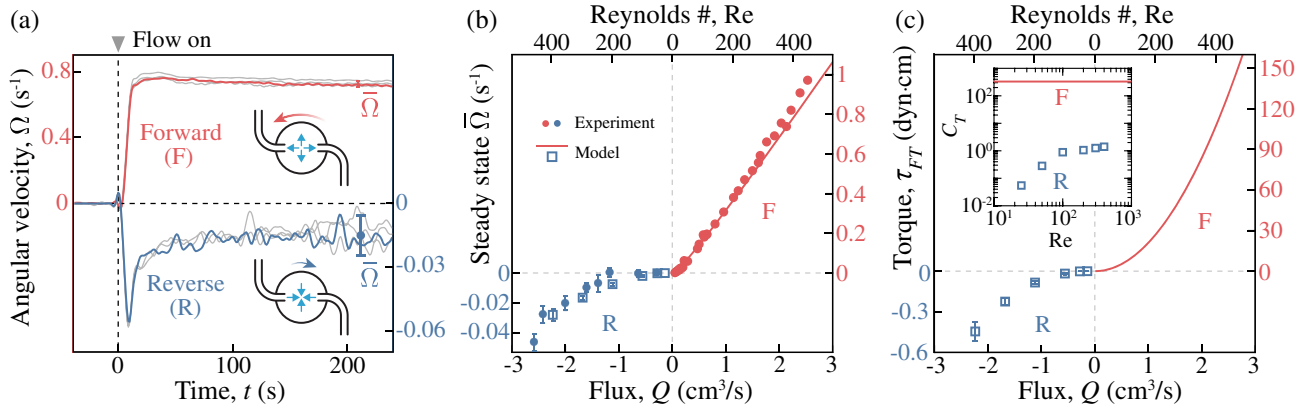

FIG. 2. Rotational dynamics in forward and reverse and across flow rates. (a) Instantaneous angular velocity $\Omega(t)$ for expulsion (red) and suction (blue) for flow of volumetric rate $|Q| = 2.0$ cm^3/s initiated at $t = 0$. The gray curves are repeated trails. (b) Long-time average or terminal velocity $\overline{\Omega}$ versus flux Q or Reynolds number Re for experiments (dots) and a model (squares). (c) Model prediction for torque τ_{FT} due to angular momentum flux. Inset: dimensionless torque coefficient C_T versus Re. In all plots, bars on experimental data represent standard deviations and are suppressed when smaller than the symbol. Bars on model data are propagated from measured fluctuations in the particle image velocimetry (PIV) flow data.

fills the hub and exits out the arms [35]. The lab-frame speed of the exhaust is slowed due to the oppositely sensed motion of the sprinkler, and this manifests as the gradual widening of the spiral-shaped streaklines. A closer view is provided in Video 6 and the time-exposed photograph of Fig. 3(b) that employs the setup of Fig. 1(c) involving laser-sheet illumination of microparticles seeded throughout the fluid [35]. Concentrating on a downward-moving outlet, an

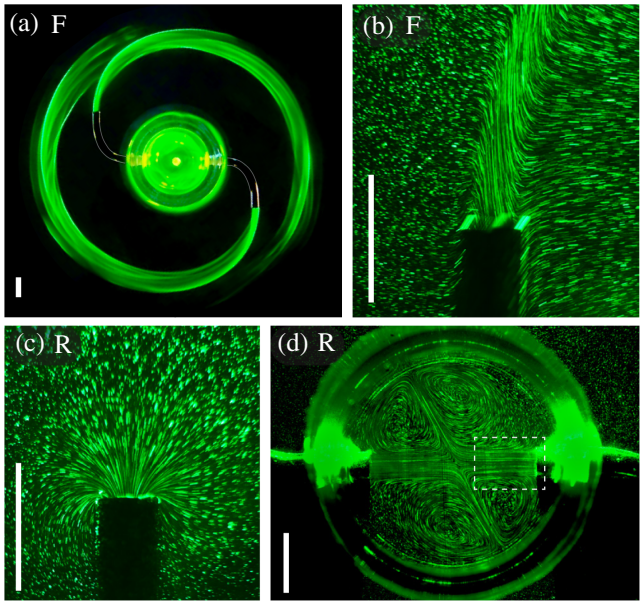

FIG. 3. Flow visualizations in the forward (F) and reverse (R) modes. All scale bars are 1 cm and flow rates $|Q| = 1$ cm^3/s. (a) Streakline photograph using fluorescein dye. (b) Pathline image of the emitted jet taken at a moment when the outlet moves downward. (c) Pathlines of the suction flow near an upward moving outlet in reverse mode. (d) The jets inside the hub undergo a glancing collision and form four vortices.

oppositely directed jet flow is revealed by the long pathlines.

Just as the conventional rocket analysis relates propulsion forces to momentum flux from the exhaust, we consider a model of the thrust torque derived from the flux of angular momentum out of the outlets. Considering the normal velocity profile $V(x, z)$ relative to an outer orifice and across its cross section, our calculations identify a flux-based thrust torque $\tau_{\mathrm{FT}} = -2\int \rho x V^2(x, z)\mathrm{d}A = 2\rho X_{OO} Q^2/3\pi a^2$. Here, X_{OO} measures the appropriate projected distance of the outer orifice from the hub center, and we assume a parabolic or Poiseuille flow profile issuing from the arms [4,5]. The derivation in the Supplemental Material employs a control volume that encloses the sprinkler with portions of its surface spanning the pipe outlets [35]. The thrust $\tau_{\mathrm{FT}}(Q)$ is plotted as the red curve in Fig. 2(c). Predicting the resulting spin rate of the sprinkler requires a model of rotational drag and its dependence on $\overline{\Omega}$. As detailed in the Supplemental Material [35], we estimate the skin friction and pressure drag contributions from the various components and surfaces of the structure [36,37]. Balancing flux-based thrust, which is reduced due to the retreating motion of the orifices, with the drag torque yields a prediction for $\overline{\Omega}(Q)$ that is plotted as the red curve in Fig. 2(b). The model shows strong agreement with the experimental measurements, indicating that the rocket mechanism quantitatively accounts for the forward mode. The linear trend $\overline{\Omega} \sim Q$ results from the scalings of thrust as Q^2 and drag as $\overline{\Omega}^2$ for high $\overline{\Omega}$.

Flux from the outlets is one of many potential contributions to thrust. The general control volume analysis [5] presented in the Supplemental Material shows that this term appears among others associated with fluxes, changes of momentum, and surface stresses [35]. Nonetheless, our model's good accounting of the forward mode motivates

the evaluation of this same source of thrust for the suction mode, whose flows are altogether different due to irreversibility. Indeed, pathline visualizations at the outer terminus of the arm [Video 7 and Fig. 3(c)], which now functions as an inlet, reveal the expected sinklike flows [35]. The functional outlets reside inside the hub, whose internal flows are visualized in Fig. 3(d). We observe a robust flow pattern consisting of four vortices separated by the two primary jets from the outlets that meet near the center of the hub and two secondary outgoing jets that are produced as a result of the collision. For increasing Re, a prominent asymmetry develops in the secondary jets, which form an increasingly large angle away from vertical. Supplemental Videos 8, 9, and 10 document this trend [35].

These observations motivate a closer interrogation of the flow exiting the pipe inside the hub. Focusing on the region indicated in Fig. 3(d), we capture high-speed video to extract time- and space-resolved maps of the flow via particle image velocimetry (PIV) [38–40]. Method details and errors are given in the Supplemental Material [35]. Figure 4(a) shows sample transects of the jet flow in a static sprinkler for appreciably large $\mathrm{Re} = 300$, revealing a strongly skewed profile with the velocity maximum displaced from the pipe centerline. Not shown is the other jet, whose skewness in the opposite direction reflects the chiral arrangement of the arms. The asymmetric primary jets meet in a glancing collision that gives rise to the angled secondary jets of Fig. 3(d). Further, the skewness becomes more pronounced with increasing Re, as documented by the extracted profiles $V(x)$ displayed in Fig. 4(b). Normalizing each by its maximum yields the curves of Fig. 4(c) that show increasingly strong asymmetries.

Considering the inner orifice of each arm as an effective outlet for the reverse sprinkler, we analyze the profiles to determine the momentum flux and thrust torque. The derivation in the Supplemental Material involves a control volume selected such that portions of its surface span the inner termini of the pipes [35]. Because we measure the flow along a transect, the velocity field over the disk-shaped surface of the outlet must be interpolated to compute the flux integral and associated thrust $\tau_{\mathrm{FT}} = -2\int \rho x V^2(x,z)\mathrm{d}A$. There is no flux and no torque for parabolic flow or any other symmetric profile, so skewness is essential. The computed torque is shown as the blue markers in Fig. 2(c), with the bars indicating fluctuations propagated from the flow measurements. The sign of the torque is set by the skewness and proves to be consistent with reverse motion. Balancing against drag yields predictions for $\overline{\Omega}(Q)$ that are shown as the open squares in Fig. 2(b). The propagated fluctuations in $\overline{\Omega}$ are of similar magnitude to those measured, suggesting that unsteady flows play a role. The time-averaged motions and nonlinear trend are well predicted, and we thus conclude that flux-based torque drives the reverse sprinkler.

The jet asymmetry is consistent with secondary flows in curved pipes that have been argued as central to the sprinkler problem [23]. Long, slender pipes of constant curvature κ—i.e., helical tubes—are well studied as the Dean flow problem [14–16,41–43], which has the controlling parameter $\mathrm{De} = \mathrm{Re}\sqrt{a\kappa}$. For De of order 10, centrifugal effects induce a transition from the typical parabolic profile to one in which the velocity maximum is displaced to the outside of the bend [44,45]. Although the sprinkler arms do not satisfy the requisite geometry, we may evaluate De by associating κ with the curvature of the elbow. Close inspection of Figs. 4(b) and 4(c) shows that $\mathrm{Re} \approx 100$–200 or $\mathrm{De} \approx 40$–80 marks the range of significant distortion, with lower values yielding symmetric flow and higher values tending to saturate on a strongly skewed profile. These trends are reflected in the torque, as made apparent by the thrust coefficient $C_T = 2\tau_{\mathrm{FT}}/\rho\bar{V}^2a^3$ plotted in the inset of Fig. 2(c). The rise and plateau of $C_T(\mathrm{Re})$ correspond respectively to the turn-on and saturation of skewness, and these effects underlie the nonlinear response of $\overline{\Omega}(Q)$ seen in Fig. 2(b).

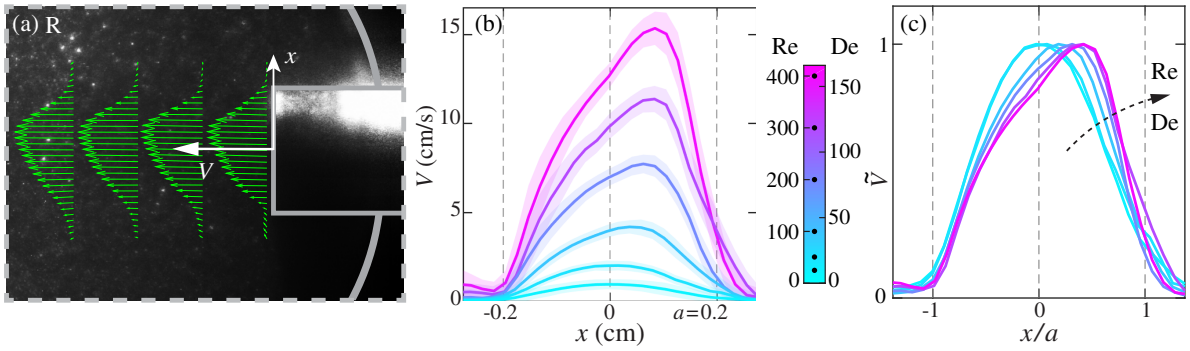

FIG. 4. Flow field measurements near the internal orifice for the reverse sprinkler. (a) Flow profiles along several transects for $\mathrm{Re} = 300$ extracted from video via particle image velocimetry (PIV). (b) Profiles $V(x)$ across the inner orifice and for varying Reynolds and Dean numbers (color bar), with temporal fluctuations (± 1 standard deviation) represented by colored bands. (c) Profiles normalized by their maximum values.

These results identify a rocketlike mechanism involving angular momentum flux from outlets as a primary source of propulsion in both modes of the sprinkler. The forward mode is a direct rotational analog to a rocket in which jets are ejected outward and circumferentially. The reverse mode is subtle due to its jets being aimed inward but which are effectively offset from one another due to their skewness. These results are shown to hold for the standard S-shaped sprinkler over $\mathrm{Re} \in [25, 400]$.

This mechanism is distinct from previous hypotheses. Rueckner associates reverse motion with a swirling flow in the hub that rotates oppositely to the sprinkler [30]. This picture relates to Mungan's earlier reports of rotation but only for designs in which the arms enter the hub nondiametrically—i.e., displaced or angled away from the center—presumably setting up an internal vortex [28]. These works report no rotation for the standard sprinkler design, a result inconsistent with our findings and which may be due to bearing friction. Rueckner claims that no vortex is present, whereas we document two pairs of counter-rotating vortices, a flow structure that we view as a side effect of the skewed jets. Our mechanism explains Mungan's variants in terms of momentum flux from internal jets. Beals cites the distorted profile for curved pipe flows to argue that pressure differences in the elbow region drive reverse rotation [23]. Jenkins had previously argued for no rotation due to two countervailing pressures [21], which Beals rebuts by asserting that forces may cancel and yet a torque is produced if the pressures are differently distributed. However, slower rotation was reported for a sprinkler variant with elongated arms [23], a result that contradicts the elbow pressure mechanism. Our mechanism predicts that such a design should indeed move slower due to symmetrization of the flow during its longer path to the hub and consequent decrease in momentum flux. Future work should revisit this design and compare experiments with model predictions.

Our results provide an answer to the Feynman sprinkler problem in a form missing from previous studies: a mechanism is translated into a concrete model whose quantitative predictions are validated against experimental measurements under documented conditions. Future studies aimed at further exploring the roles of Reynolds number and sprinkler geometry would benefit from such an approach and from the methods developed here.

We thank B. Griffith, A. Mincer, C. Peskin, and J. Zhang for helpful discussions, the NSF for financial support (DMS-1646339), and especially A. Donev for his inspiration and mentorship.

*Corresponding author: ristroph@cims.nyu.edu

[1] R. P. Feynman and R. Leighton, *"Surely You're Joking, Mr. Feynman!": Adventures of a Curious Character* (Random House, New York, 1992).
[2] J. A. Wheeler, Phys. Today **42**, No. 2, 24 (1989).
[3] E. Creutz, Am. J. Phys. **73**, 198 (2005).
[4] D. J. Tritton, *Physical Fluid Dynamics* (Springer Science & Business Media, New York, 2012).
[5] F. M. White, *Fluid Mechanics* (Tata McGraw-Hill Education, New York, 1979).
[6] O. De Vries, Annu. Rev. Fluid Mech. **15**, 77 (1983).
[7] E. Mach, *The Science of Mechanics* (The Open Court Publishing Co., Chicago, 1919).
[8] H. Cui and J. Tani, JSME Int. J. Ser. C **39**, 20 (1996).
[9] A. Glezer and M. Amitay, Annu. Rev. Fluid Mech. **34**, 503 (2002).
[10] G. Kuiper and A. Metrikine, J. Sound Vib. **280**, 1051 (2005).
[11] T. B. Benjamin, Proc. R. Soc. A **261**, 457 (1962).
[12] M. P. Paidoussis, *Fluid-Structure Interactions: Slender Structures and Axial Flow* (Academic Press, New York, 1998), Vol. 1.
[13] A. Hellum, R. Mukherjee, and A. J. Hull, J. Fluids Struct. **27**, 1086 (2011).
[14] W. Collins and S. Dennis, Q. J. Mech. Appl. Math. **28**, 133 (1975).
[15] S. Berger, L. Talbot, and L.-S. Yao, Annu. Rev. Fluid Mech. **15**, 461 (1983).
[16] M. Ghobadi and Y. S. Muzychka, Heat transfer engineering **37**, 815 (2016).
[17] A. T. Forrester, Am. J. Phys. **54**, 798 (1986).
[18] E. R. Lindgren, Am. J. Phys. **58**, 352 (1990).
[19] A. K. Schultz, Am. J. Phys. **55**, 488 (1987).
[20] M. R. Collier, R. E. Berg, and R. A. Ferrell, Am. J. Phys. **59**, 349 (1991).
[21] A. Jenkins, Am. J. Phys. **72**, 1276 (2004).
[22] A. Jenkins, Eur. J. Phys. **32**, 1213 (2011).
[23] J. Beals IV, Am. J. Phys. **85**, 166 (2017).
[24] A. T. Forrester, Am. J. Phys. **55**, 488 (1987).
[25] L. Hsu, Am. J. Phys. **56**, 307 (1988).
[26] S. Dasgupta, P. Mitra, and S. Sengupta, Eur. J. Phys. **11**, 311 (1990).
[27] M. Kuzyk, Phys. Today **42**, No. 11, 127 (1989).
[28] C. Mungan, Phys. Teacher **43**, L1 (2005).
[29] M. P. Païdoussis and M. Tétreault-Friend, Am. J. Phys. **77**, 349 (2009).
[30] W. Rueckner, Am. J. Phys. **83**, 296 (2015).
[31] R. E. Berg and M. R. Collier, Am. J. Phys. **57**, 654 (1989).
[32] P. A. Kralchevsky and K. Nagayama, Langmuir **10**, 23 (1994).
[33] N. Bowden, I. S. Choi, B. A. Grzybowski, and G. M. Whitesides, J. Am. Chem. Soc. **121**, 5373 (1999).
[34] H. Cooray, P. Cicuta, and D. Vella, J. Phys. Condens. Matter **24**, 284104 (2012).
[35] See Supplemental Material at http://link.aps.org/supplemental/10.1103/PhysRevLett.132.044003 for details of the methods and supporting calculations.
[36] H. Schlichting and J. Kestin, *Boundary Layer Theory* (Springer, New York, 1961), Vol. 121.
[37] B. R. Munson, D. F. Young, T. H. Okiishi, and W. W. Huebsch, *Fundamentals of Fluid Mechanics* (Wiley, New York, 2006).

[38] E. Stamhuis and W. Thielicke, J. Open Res. Software **2**, 30 (2014).
[39] W. Thielicke, The Flapping Flight of Birds—Analysis and Application Ph.D. thesis, Rijksuniversiteit Groningen (2014), 10.13140/RG.2.2.18656.94728.
[40] W. Thielicke and R. Sonntag, J. Open Res. Software **9**, 12 (2021).
[41] W. R. Dean, London, Edinburgh, Dublin Philos. Mag. J. Sci. **4**, 208 (1927).
[42] W. Dean, Philos. Mag. **5**, 673 (1928).
[43] H. Topakoglu, J. Math. Mech. **16**, 1321 (1967).
[44] C. White, Proc. R. Soc. A **123**, 645 (1929).
[45] H. Itō, J. Basic Eng. **81**, 123 (1959).